https://doi.org/10.5194/egusphere-2026-2868
Preprint. Discussion started: 12 June 2026

Infrared-radiofluorescence in feldspar: grain-scale mineralogy and its effect on dose response curves and apparent saturation

Taylor Grandfield[1], Mariana Sontag-González[2], Raju Kumar[2,3], Juergen Thieme[1,4], Andrew M. Kiss[5], Jean-Luc Schwenninger[2], Victoria Castle[1], Hanna Nekvasil[1], Marine Frouin[1,6]

[1] Department of Geosciences, Stony Brook University, 255 Earth and Space Sciences Building, Stony Brook, NY 11794, USA
[2] Research Laboratory for Archaeology and the History of Art, University of Oxford, Dyson Perrins Building, 1 South Parks Road, OX1 3TG, Oxford, UK
[3] Department of Geology and Geophysics, Indian Institute of Technology (IIT), Kharagpur-721302, West Bengal, India
[4] Institute for X-Ray Physics, Georg August University of Goettingen, Germany
[5] National Synchrotron Light Source II, Brookhaven National Laboratory, Upton, New York 11973, USA
[6] Turkana Basin Institute, Stony Brook University, N507A Social & Behavioral Sciences, Stony Brook, NY 11794-436, USA

Correspondence to: Taylor Grandfield (taylor.grandfield@stonybrook.edu)

Abstract

Infrared radiofluorescence (IR-RF) dating of K-feldspar is commonly performed on multi-grain aliquots, implicitly treating the IR-RF dose response curve (DRC) and its apparent saturation behavior as properties of a sample. Here, we test the alternative hypothesis that bulk DRC curvature and plateau dose can emerge from mixtures of grains with contrasting mineralogy and luminescence behavior. We combine (i) single-grain, multi-spectral RF measurements (710, 850, 880 nm) on feldspar reference materials spanning the ternary diagram, (ii) controlled mixed-grain aliquot experiments using a detection window centered at 850 nm, (iii) spatially resolved IR-RF (SR IR-RF) imaging of natural samples (X7363, X7368) using an RF_{70} style protocol and grain-scale DRC classification, and (iv) synchrotron-based μ-XRF mapping at 10 keV to assess grain-scale chemistry and evaluate surface versus interior controls.

Reference measurements confirm strong dependence of IR-RF behavior on feldspar type and polymorph. Albite and microcline commonly show high initial intensities and decaying DRCs at 850-880 nm, whereas Ca-rich feldspars are weak and near-flat, and sanidine exhibits variable, sometimes increasing DRCs. Mixing experiments demonstrate that adding a small number of grains with contrasting behavior measurably shifts microcline DRC curvature and reduces apparent saturation. SR IR-RF reveals that both natural samples tested contain grains with decreasing, increasing, and near-flat regenerative DRCs, and that polishing produces minimal change in DRC shape, arguing against a purely surface-controlled origin for anomalous behavior. Qualitative 10 keV μ-XRF maps show that grain-scale elemental detections and spatial patterns do not uniquely

https://doi.org/10.5194/egusphere-2026-2868
Preprint. Discussion started: 12 June 2026

predict the DRC category, implying that IR-RF behavior is not controlled by composition alone. For dating purposes, these results imply that saturation limits and equivalent dose estimates should not be inferred from averaged signals in heterogeneous samples, particularly those of volcanic origin. We propose a practical two-step screening workflow that combines DRC-shape classification with the dose corresponding to 95% of the fitted asymptotic level (D95) to prioritize high-capacity grains. This approach now requires validation on independently well-dated and/or stratigraphically constrained sequences.

1 Introduction

Introduced in 1999, IR-RF dating of K-feldspar emerged as an alternative luminescence approach that uses ionizing irradiation instead of optical stimulation (Trautmann et al., 1998; Trautmann et al., 1999; Schilles and Habermann, 2000). During continuous irradiation, K-feldspars emit an infrared radiofluorescence band that was first reported near 1.44 eV (~855 nm) (Trautmann et al., 1998), later refined to ~1.43 eV (~865 nm) (Erfurt and Krbetschek, 2003 a, b), and more recently measured around ~880 nm (Kumar et al., 2018; Riedesel et al., 2021; Sontag-González et al., 2022). For simplicity and consistency with previous studies, we retain the 865 nm designation for this work.

The signal is interpreted as being associated with electron trapping during irradiation: as the number of available traps decreases with absorbed dose, the IR-RF intensity follows a decreasing stretched exponential fit, consistent with models in which IR-RF intensity is proportional to the probability of electron trapping (Trautmann et al., 2000; Erfurt and Krbetschek, 2003a). Erfurt and Krbetschek (2003a) were the first to formalize a single-aliquot regenerative dose protocol (SAR) for IR-RF, termed IR-SAR, to determine the equivalent dose (D_e). In this approach, the D_e is obtained through three main steps: (1) measure the IR-RF signal during an additive irradiation, (2) optically bleach the aliquot to empty the traps and allow a pause to avoid post-bleach phosphorescence, and (3) measure the regenerated IR-RF signal during a second irradiation. The D_e is obtained directly by sliding the natural IR-RF curve onto the regenerated curve; dividing D_e by the environmental dose rate provides the burial age (Kreutzer et al., 2017; Murari et al., 2021).

IR-RF methodological work following the development or IR-SAR protocols has largely focused on two factors that strongly influence the D_e estimation: bleaching behavior and temperature dependence during irradiation and measurement (Trautmann et al., 1999; Krbetschek et al., 2000; Buylaert et al., 2012; Frouin et al., 2017). Building on this early work, an improved single-aliquot regenerative protocol (RF_{70}) was proposed in 2017, relying on IR-RF measurements and bleaching conducted at elevated temperature to stabilize the measurement conditions and limit the contribution of very shallow traps (Huot et al., 2015; Frouin et al., 2017).

More recent studies increasingly examine the information contained in the IR-RF dose response curve (DRC) itself, including its relation to trap filling dynamics, signal saturation, and grain-scale variability (e.g., Mittelstraß and Kreutzer, 2021;

https://doi.org/10.5194/egusphere-2026-2868
Preprint. Discussion started: 12 June 2026

Kreutzer et al, 2022; Sontag-González et al., 2024). At the onset of the DRC, the signal intensity is high because the proportion of trapped electrons is low and the probability of trapping newly created charge during irradiation is therefore maximal. With increasing dose, the available trap population decreases, and the IR-RF signal follows a monotonic decay toward a plateau. This behavior reflects the progressive filling of the dosimetric traps during irradiation and is consistent with the interpretation that IR-RF intensity is proportional to the probability of electron trapping. The high-dose region corresponds to trap saturation for the relevant trap system under the applied protocol. Beyond this point, additional dose produces little change in signal intensity, so the plateau defines the maximum measurable D_e and therefore the upper age limit accessible with the IR-RF signal.

Traditionally, IR-RF measurements have been conducted on multi-grain aliquots, typically composed of tens to hundreds of K-rich feldspar grains, and the resulting signal reflecting the integrated response of the grain population (e.g., Trautmann et al., 2000; Frouin et al., 2017). However, several studies have shown that IR-RF characteristics vary substantially at the single-grain scale, and that this variability is largely averaged out in multi-grain measurements (Frouin et al., 2017; Mittelstraß and Kreutzer, 2021). As a result, this averaging can mask the presence of grains with different saturation characteristics potentially biasing D_e estimates when only multi-grain aliquots are considered. These observations motivate a systematic investigation of IR-RF behavior at the single-grain level.

A growing body of work, including recent results from our group, suggests that this grain-scale variability is, at least in part, geochemically controlled. Synchrotron-based micro-X-ray fluorescence (μ-XRF) mapping of individual K-feldspar grains demonstrated that grains from the same K-rich feldspar density fraction (<2.58 $g.cm^{-3}$) can display markedly different IR-RF dose response behavior, suggesting that grain-scale compositional heterogeneity influences luminescence characteristics (Sontag-González et al., 2024). Trace-element enrichments, particularly in elements such as lead (Pb), barium (Ba), iron (Fe), or calcium (Ca), were found to correlate with differences in signal intensity and dose response shape, consistent with their role as activators or quenching centers in feldspar luminescence systems (e.g., Kumar et al., 2020). These studies showed that some grains produce weak, noisy, or anomalous responses. Contamination from non-K-rich feldspar phases can explain part of this variability. The origin of the observed differences remains unclear, especially with respect to intrinsic grain-scale chemistry and defect structure.

Spatially resolved IR-RF measurements using CCD-based imaging have further confirmed pronounced grain-to-grain variability and demonstrated that single-grain IR-RF dating is technically feasible (Mittelstraß and Kreutzer, 2021; Kumar et al., 2026). Together, these developments indicate that the shape of the IR-RF DRC carries information about trap populations and mineral chemistry that cannot be recovered from multi-grain measurements alone.

https://doi.org/10.5194/egusphere-2026-2868
Preprint. Discussion started: 12 June 2026

The present study builds on this progression by directly correlating single-grain geochemistry with IR-RF dose response behavior. Our overall goal is to improve the robustness of IR-RF dating by investigating the effect of possible inclusions or contamination of the K-rich feldspar density fraction. Here, our objectives are to (1) evaluate the relationship between DRC shape and grain-scale composition, (2) determine how mixtures of feldspar endmembers influence the apparent saturation and dynamic range of mixed-mineral aliquots, and (3) test whether luminescence heterogeneity is restricted to grain surfaces or extends throughout crystal interiors.

To address these questions, we combine conventional PMT-based RF measurements with spatially resolved (SR) IR-RF imaging and synchrotron based μ-XRF mapping at the Submicron Resolution X-ray Spectroscopy (SRX) beamline (NSLS-II, Brookhaven National Laboratory). Measurements were conducted at the single-grain level using multi-filter detection centered near 710, 850, and 880 nm to characterize emission components associated with different trap systems. Synthetic multi-grain aliquots were prepared with different feldspar endmembers spanning the ternary feldspar system to quantify mixing effects on the dose response behavior. In parallel, natural samples and reference feldspars were analyzed with SR-IR-RF and μ-XRF mapping to determine whether anomalous IR-RF signals arise from surface coatings, inclusions, or intrinsic crystal-scale compositional heterogeneity.

2 Materials and Methods

2.1 Reference Samples

We selected a suite of eight feldspar reference samples to span a broad range of compositions across the sodium (Na), Ca-, and K-feldspar compositions. Reference samples were obtained from the Smithsonian Microbeam and Stony Brook University (SBU) collections and consist of coarse, single-crystal grains spanning the feldspar ternary system.

The plagioclase samples used were: SBU Amelia Albite ($An_0Ab_{98}Or_2$), anorthite NMNH 137041 ($An_{95}Ab_5Or_0$, Jarosewich, 1980; Jarosewich, 2002), and labradorite NMNH 115900 ($An_{68}Ab_{31}Or_1$, Jarosewich, 1980; Jarosewich, 2002). The K-rich feldspars used varied not only in composition but also in structure, degree of Al-Si ordering, and formation temperature. Sanidine is a monoclinic, high-temperature K-feldspar associated with rapidly cooled volcanic rocks and poor Al-Si ordering (e.g., Ribbe, 1983). Orthoclase is a monoclinic K-feldspar associated with low to medium temperature conditions and intermediate structural ordering. Microcline is the triclinic, low-temperature K-feldspar generally associated with slower cooling and exhibits greater Al-Si ordering. The effects of feldspar polymorphism and compositional mixing on the IR-RF signal behavior remain poorly constrained, particularly when feldspars contain complex intergrowths, such as perthitic exsolution. To explore this, we used reference microcline NMNH 143966 ($An_0Ab_{12}Or_{88}$, Jarosewich, 1980; Jarosewich, 2002), and the well-characterized Fish Canyon Tuff sanidine (FCs; Cebula et al., 1986), $An_1Ab_{24}Or_{75}$ (Zimmerer and McIntosh, 2011).

https://doi.org/10.5194/egusphere-2026-2868
Preprint. Discussion started: 12 June 2026

Three additional sanidine samples from the Alder Creek Rhyolite (ACs; Turrin et al., 1994), Taylor Creek Rhyolite (TCs; Duffield and Dalrymple, 1990), and Peach Springs Tuff (Cima; Nielsen et al., 1990) were also used. Although compositional data are not available for these three samples, they are identified as sanidine in the literature and are therefore treated as sanidine for the purposes of this experiment. Compositional information for the albite, anorthite, labradorite, microcline, and FCs samples is provided in Supplementary Table S1.

2.2 Natural Samples

We selected two natural samples of interest from the Turkana Basin, Kenya (X7363 and X7368) that were previously investigated in our group's synchrotron-based study (Sontag-González et al., 2024); here we report additional measurements on the same natural samples. Sample X7363 was collected from the Gele Tuff in the Turkana Basin, Kenya, which was previously dated by $^{40}Ar/^{39}Ar$ geochronology to 1.31 ± 0.002 Ma (Philips et al., 2023). Sample X7368 was collected from a sediment package stratigraphically below the undated Kale Tuff and above the Silbo Tuff, which has been dated by $^{40}Ar/^{39}Ar$ geochronology to 0.751 ± 0.002 Ma (McDougall and Brown, 2006). These samples were selected both for their significant to Pleistocene contexts in the Turkana Basin and their interesting IR-RF characteristics.

2.3 Sample Preparation

The single crystal grains of the reference samples were directly used without any additional sample preparation. For the natural samples, sample preparation was carried out at the Luminescence Dating Laboratory of the School of Archaeology, at the University of Oxford, under controlled low-intensity amber (594 nm) lighting conditions. Sediments were wet sieved after an ultrasonic bath for 10 min to isolate the 185-255 µm size fraction. This fraction was then chemically treated with hydrochloric acid (10% HCl) and hydrogen peroxide (30% H_2O_2) for 72 hrs to remove carbonates and organic matter, respectively. Mineral separation was then performed using sodium polytungstate (SPT) heavy liquid at a density of 2.58 $g.cm^{-3}$ to isolate the K-rich feldspar density fraction. The K-rich feldspar density fraction was then re-sieved to remove any material < 185 µm.

2.4 Synchrotron based µ-XRF

Assessing the composition of the phases used is a vital first step in this study. Sontag-González et al.(2024) successfully applied synchrotron-based µ-XRF maps and µ-X-ray Absorption Near-Edge Structure (XANES) measurements of individual grains in the same K-rich feldspar density fraction analyzed for IR-RF dating at the Submicron Resolution X-ray Spectroscopy beamline (SRX; 5-ID) of the NSLS-II (Nazaretski et al., 2022). Using an excitation energy of 13.5 keV, they targeted trace elements such as Fe and Pb and suggested that grain-to-grain geochemical variability coincides with differences in the IR-RF dose response behavior. Grains enriched in K together with trace amounts of Pb and Ba typically produced IR-RF curves that decrease exponentially with dose; grains containing a higher proportion of Fe, and in some cases Ca (likely present as an anorthite component), often produced weak signals, noisy behavior, or curves that increase with dose rather than decay. These

https://doi.org/10.5194/egusphere-2026-2868
Preprint. Discussion started: 12 June 2026

observations are consistent with the interpretation that trace elements such as Pb or Ba may enhance IR-RF emission, while Fe (particularly Fe^{3+}) may introduce competing emission centers or quenching processes that modify the observed DRC shape (Kirsh and Townsend, 1988; Krbetschek et al., 2000; Erfurt and Krbetschek, 2003; Jain et al., 2015; Frouin et al., 2019; Kumar et al., 2020; Sontag-González and Fuchs, 2022). However, the precise role of Fe remains uncertain, as elevated Fe signals may also reflect surface contamination (e.g., surface coatings) rather than an intrinsic lattice substitution.

Building on this work, we acquired high-resolution µ-XRF maps, also at NSLS-II SRX (5-ID), at 10 keV to improve sensitivity and signal-to-noise for elements with lower K-edge energies that are abundant in feldspars, particularly K, Ca, and Fe. When the excitation energy is substantially higher than the absorption edge of an element, the fluorescence yield relative to the scattering background decreases and the corresponding peaks become less distinct. Selecting an energy closer to the relevant edges therefore improves detection of these elements and allows clearer identification of spatial variations in their distributions. This is important because Ca and Fe are observed preferentially in grains with anomalous IR-RF behavior (Sontag-González et al., 2024), and improved sensitivity to these elements enables an evaluation of whether such behavior reflects intrinsic compositional heterogeneity rather than trace-element contamination alone.

In this study, µ-XRF maps are used to qualitatively identify elemental distributions within and between grains. Very low-Z elements such as aluminum (Al), silicon (Si), and sodium (Na) cannot be detected with this configuration because their fluorescence lines are strongly attenuated in air. Therefore, our analyses focus on elements detectable at 10 keV. The incident X-ray beam was focused using a Kirkpatrick-Baez mirror system. The µ-XRF maps were obtained by scanning the entire grain (~250 µm diameter), with a step size of 1 µm and an integration time ranging from 0.1 to 0.025 s per image pixel. Each element's characteristic fluorescence signal was collected from the total signal of a seven-element silicon drift detector (Hitachi Vortex ME-7) and normalized to the incident X-ray flux (I_0). Data reduction and map generation were carried out using the open-source software PyXRF v.1.0.28 (Li et al., 2017).

2.5 Luminescence Devices

2.5.1 SBU Lexsyg Research Device

The SBU Luminescence Dating Research Laboratory is equipped with a Freiberg Instruments *Lexsyg Research* device (Richter et al., 2013), aka 'Ghost', equipped with a $^{90}Sr/^{90}Y$ ring shaped beta irradiation source (Richter et al., 2012) delivering a dose rate of 0.202 ± 0.006 $Gy.s^{-1}$ to the material deposited on the stainless-steel cup at the time of calibration (March 2025) using Risø calibration quartz batch 204 (250-180 µm). The device is equipped with two photomultiplier tubes (PMT), one allowing Optically Stimulated Luminescence (OSL), Thermoluminescence (TL), and Infrared photoluminescence (IRPL) detection (Hamamatsu H7421-50) and one allowing RF detection (Hamamatsu H7360-02) placed above the source. The reader is equipped with a series of bandpass interference filters allowing RF detection centered in the red part of the spectrum at 710

https://doi.org/10.5194/egusphere-2026-2868
Preprint. Discussion started: 12 June 2026

nm (Edmund Optics 710/10 #67-839), near IR at 850 nm (Chroma 850/30 filter), and at 880 nm (Edmund Optics 880/10 #65-183) (Fig. S1a). The 710 nm filter isolates the red emission component, which has been reported to increase rapidly with dose and to exhibit strong light sensitivity. The 850 nm filter targets the central portion of the ~865 nm IR-RF emission band, while the 880 nm filter isolates the longer-wavelength near-infrared component of the IR-RF signal. A built-in solar simulator equipped with different LEDs at: 365 nm, max. 52 mW cm^{-2}; 462 nm, max. 196 mW cm^{-2}; 525 nm, max. 62 mW cm^{-2}; 590 nm, max. 51 mW cm^{-2}; 625 nm, max. 118 mW cm^{-2}; 850 nm, max. 236 mW cm^{-2}, was used for bleaching the aliquots during the IR-SAR measurements. The generated data (.xsyg files) were then analyzed using the function read_XSYG2R() v.0.6.15 from the R 'Luminescence' package v.1.1.0 (Kreutzer et al., 2025).

2.5.2 Oxford Lexsyg Research Device

The Oxford Luminescence Dating (OLD) Laboratory at the University of Oxford is equipped with a Freiberg Instruments *Lexsyg Research* device (Richter et al., 2013), equipped with a $^{90}Sr/^{90}Y$ ring shaped beta irradiation source (Richter et al., 2012) delivering a dose rate of 0.043 ± 0.001 $Gy.s^{-1}$ to the material deposited on the stainless-steel cup at the time of calibration (October 2025) using Risø calibration quartz batch 204 (250-180 µm). The reader is equipped with a series of bandpass interference filters coupled with plano-convex lenses allowing RF detection centered in the red part of the spectrum at 710 nm (Thorlabs FBH710/10 and Edmund Optics uncoated plano-convex lens #48-274), near IR at 850 nm (Chroma D850/40 and Edmund Optics NIR-I coated plano-convex lens #18-070), and 880 nm (Edmund Optics 880/10 and Edmund Optics uncoated plano-convex lens #48-274) (Fig. S1b). For bleaching, the built-in solar simulator equipped with different LEDs was used: 365 nm, max. 70 mW cm^{-2}; 462 nm, max. 110 mW cm^{-2}; 525 nm, max. 45 mW cm^{-2}; 590 nm, max. 30 mW cm^{-2}; 625 nm, max. 90 mW cm^{-2}; 850 nm, max. 170 mW cm^{-2}.

While the device was originally purchased in 2014, it received an upgrade in 2025, described and tested in Kumar et al. (2026) to enable SR IR-RF by integrating an Andor iKon-M 934 CCD camera with custom optics at the IR-RF position. Built by Freiberg Instruments, the system uses a 1024×1024 pixel, 13 µm pitch, back-illuminated deep-depletion sensor (BEX2-DD), giving high quantum efficiency (> 80%) across 380-900 nm. All operations are automated via LexStudio2 software. The camera runs at a 5 MHz pixel readout rate, transferring frames in ~0.2 s/frame, with exposure times adjusted to avoid frame loss. Images are typically acquired in 2×2 binned mode, digitized at 16-bit depth, and the detector is cooled to -80 °C to suppress thermal noise. The SR IR-RF measurements were carried out following an IR-SAR measurement protocol, RF_{70} (Frouin et al., 2017), adapted for SR IR-RF measurements by Kumar et al. (2026).

The generated SR IR-RF datasets were analyzed in ImageJ using the SR-RF macro, following the data processing techniques developed by Mittelstraß and Kreutzer (2021). The resulting processed data (*. rf files) were then analyzed using

https://doi.org/10.5194/egusphere-2026-2868
Preprint. Discussion started: 12 June 2026

the function read_RF2R() v.0.1.1 and analyse_IRSAR.RF() v.0.7.10 from the R 'Luminescence' package v.1.1.0 (Kreutzer et al., 2025).

3 Results

3.1 µ-XRF mapping

3.1.1 µ-XRF mapping of reference samples

Five µ-XRF maps were collected for the whole grain reference feldspar samples of interest at 10 keV. The whole grains of each reference sample were mounted into a resin single-grain sample holder. Control µ-XRF measurements of the sample holder showed negligible trace-element background, indicating that holder contributions to the grain maps were very minimal (Fig. S2). The µ-XRF mapping of the reference feldspar samples identified up to twelve elements in the 10 keV spectra (Fig. 1). The absence of Na and Al reflects the experimental limitations at the SRX beamline rather than the composition of the samples themselves. While the grain's topography and thickness prevent direct comparison of relative intensities and concentrations, here we focus on the presence and absence of elements in the µ-XRF maps (Fig. 1) along with the spatial distributions of each element detected at 10 keV (Fig S3-7).

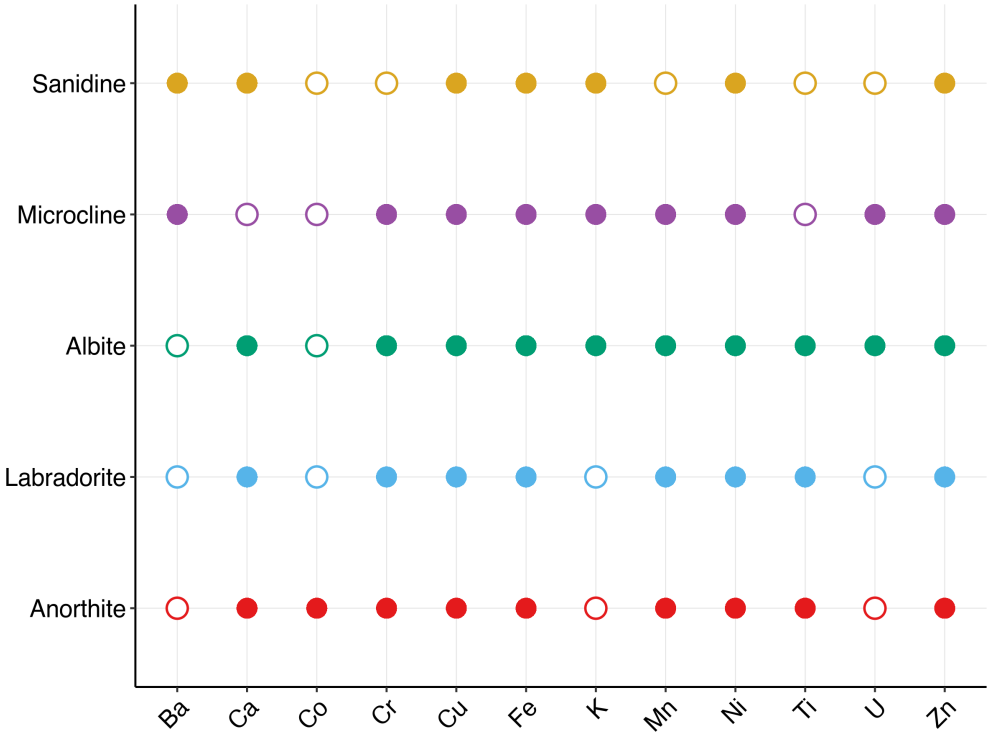

https://doi.org/10.5194/egusphere-2026-2868
Preprint. Discussion started: 12 June 2026

Figure 1: Elements detected across each reference sample at 10 keV (microcline: purple, albite: green, anorthite: red, labradorite: blue, sanidine: yellow). Filled circles indicate the presence of the element, while hollow circles indicate the absence of an element for the 10 keV experimental setup.

The microcline sample displays a homogeneous distribution of K, Ba, Ca, and uranium (U) throughout the grain, whereas Fe, zinc (Zn), chromium (Cr), manganese (Mn), and nickel (Ni) occur as discrete small inclusions (Fig. S3). The albite sample shows fewer apparent features, due to the lack of Na detection (Fig. S4). However, K appears to be distributed homogeneously throughout the sample, while the remaining elements appear as localized spots. For the labradorite sample, Ca, Fe, Mn, and V are evenly distributed across the sample, whereas Cr, copper (Cu), Ni, titanium (Ti), and Zn occur as sporadic point features (Fig S5). While in the anorthite grain, Ca and Ni are homogeneously found throughout the grain, the remaining elements are very small discrete inclusions (Fig S6). The sanidine (FCs) sample exhibits a homogenous distribution of K, Ba, and Ca throughout the grain, with Fe and Zn present as more discrete inclusions (Fig S7). Overall, the feldspar grains show distinct elemental distribution patterns, and the variations in K, Ca, and Fe reflect underlying differences in their bulk geochemistry.

3.1.2 µ-XRF mapping of natural samples

A total of thirty-two µ-XRF maps were generated for the natural feldspar samples (X7363 and X7368), including fourteen whole grain maps for X7363 and nine for X7368. The mapping of the two samples identified up to 12 elements in the 10 keV spectra (Fig. 2). Each grain's thickness and topography prevent the direct comparison of relative intensities and concentrations of each element. Here, we focused on the presence and absence of elements in µ-XRF spectra collected at 10 keV for comparison with the reference feldspar samples. All grains contained detectable Ca, Fe, Ti, and Zn. K was present in all but one grain, which instead represented a similar elemental make up to the anorthite reference sample, minus the presence of Ba (again, Na was not analyzed).

https://doi.org/10.5194/egusphere-2026-2868
Preprint. Discussion started: 12 June 2026

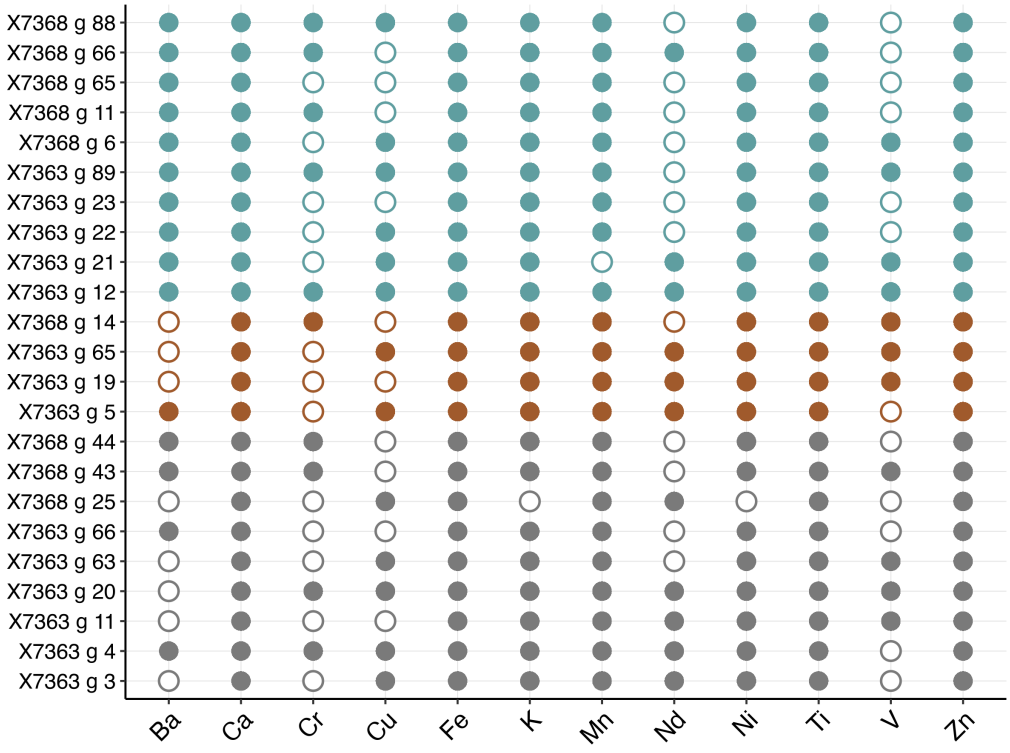

Figure 2: Elements detected within individual grains from the natural samples, X7363 (Gele Tuff, Turkana Basin, Kenya) and X7368 (Sediment package below the Kale Tuff and above the Silbo Tuff, Turkana Basin, Kenya) K-rich feldspar density fraction, measured at 10 keV distinguished by IR-RF DRC category: 1 (blue), 2 (rust), and 3 (grey). Filled circles indicate element presence and hollow circles indicate absence for the 10 keV experimental setup.

After the whole grain measurements were completed, the samples were polished to remove any surface coating and expose the composition of the grain's interior. Eleven grains were then selected for re-analysis using the same µ-XRF measurement strategy, including seven grains from X7363 and four grains from sample X7368. Figure 3 presents µ-XRF maps for three individual grains from sample X7363, shown for both the whole and polished grains. From the maps, we observe that Fe is primarily confined to the surface of the grains, consistent with an Fe-rich surface coating. At 10 keV, the interiors of the grains appear dominated by either K or Ca.

Overall, the comparison between the whole-grain and polished-grain analyses suggests that for our purposes, the surface coatings does not alter the apparent bulk geochemistry for the grains. However, both analyses reveal a clear compositional separation between certain grains, reinforcing the potential for different compositional solid solutions being present within the sample, particularly sanidine grains within the K-rich feldspar density fraction of our samples. However,

https://doi.org/10.5194/egusphere-2026-2868
Preprint. Discussion started: 12 June 2026

the μ-XRF results need to be interpreted alongside the IR-RF results to assess if the compositional differences between natural and reference samples alight with variability of the IR-RF signal.

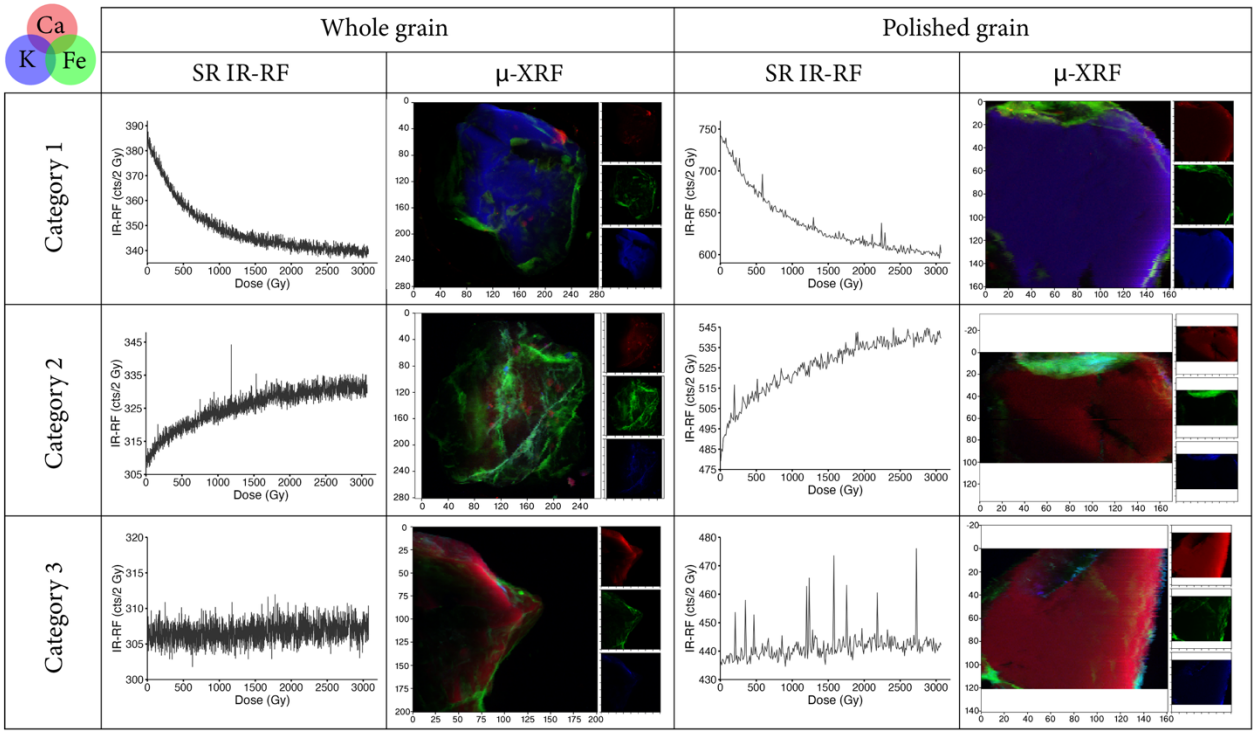

Figure 3: SR-RF (850/40 nm filter) and μXRF maps for the same grains pre- and post-polishing for category 1 (top), 2 (center), and 3 (bottom) grains for the K-rich feldspar density fraction of sample X7363 (Gele Tuff, Turkana Basin, Kenya). μ-XRF maps are shown as RBG composites, where red = calcium (Ca), green = iron (Fe), and blue = potassium (K); inset panels show the corresponding single-element maps. The μ-XRF map axes are given in pixels, with a spatial resolution of 1 μm per pixel.

3.2 Single grain IR-RF dose response curve

3.2.1 Multi-spectral measurements

Dose response curves were measured for the reference set of feldspar samples. RF measurements of individual grains manually placed on stainless steel cups were performed using three detection filters centered at 710, 850, and 880 nm. Measurements were carried out at 70 °C following the protocol of Frouin et al. (2017), with irradiation continued up to a total dose of 12,000 Gy. For all three filters, each feldspar reference sample produced an IR-RF signal above background (Fig. 4a-c).

https://doi.org/10.5194/egusphere-2026-2868
Preprint. Discussion started: 12 June 2026

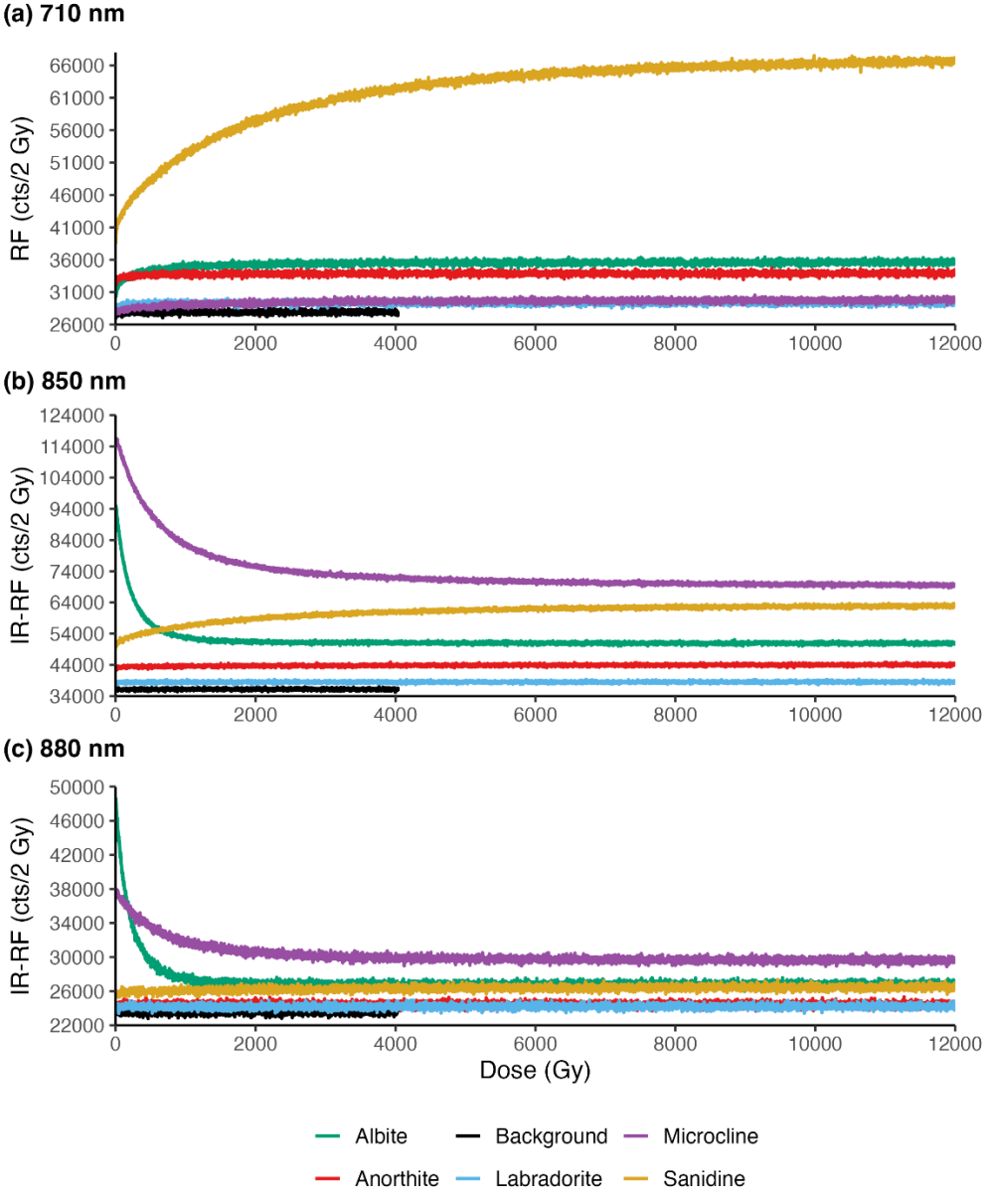

Figure 4: Multi-spectral measurements of reference feldspars detected through (a) 710 nm filter, (b) 850 nm filter, and (c) 880 nm filter. Albite is plotted in green, anorthite in red, labradorite in blue, microcline in purple, and sanidine (TCs) in yellow. The background measurement was obtained from an empty sample holder and is illustrated in black.

At 710 nm (Fig. 4a), albite shows a sharp increase in RF intensity with dose, reaching a plateau near ~1000 Gy. Anorthite increases more gradually and at lower intensity, approaching a plateau near ~500 Gy. Labradorite exhibits a low signal that rises slightly over the first ~100 Gy before reaching a plateau by ~200 Gy. Microcline displays a progressive

https://doi.org/10.5194/egusphere-2026-2868
Preprint. Discussion started: 12 June 2026

increase over the full dose range without reaching a clear plateau, whereas sanidine (TCs) shows the highest intensity, increasing with dose and approaching a plateau near ~10 000 Gy.

At 850 nm (Fig. 4b), albite shows a sharp decrease in IR-RF intensity with dose, approaching a plateau near ~800 Gy. Anorthite and labradorite exhibit low-intensity signals that remain near-flat across the measured dose range. Microcline displays a gradual decrease toward a plateau near ~4000 Gy. In contrast, sanidine (TCs) shows an increase in IR-RF intensity with dose, approaching a plateau near ~2000 Gy.

At 880 nm (Fig. 4c), albite again shows a high initial intensity followed by a decrease toward a plateau near ~500 Gy. Anorthite and labradorite remain near background levels. Microcline shows a broader decrease with dose, approaching a plateau near ~2000 Gy, while sanidine (TCs) displays a low signal that decreases slightly and reaches a plateau near ~500 Gy.

Across the three detection windows, all feldspar samples show increasing RF intensity with dose at 710 nm, whereas responses at 850 and 880 nm include decreasing, near-flat, and increasing curves depending on the sample. An increasing IR-RF signal with dose does not reflect the behavior expected for the principal IR-RF traps. In IR-RF, the signal intensity is proportional to the probability that newly created charge is captured by empty traps; as traps fill during irradiation, the signal should decrease and approach a plateau. Therefore, a monotonic increase with dose indicates that an additional emission component contributes to the measured signal. Multi-spectral studies of K-feldspar RF have shown that the red emission near ~710 nm behaves differently from the main IR-RF band near 850-880 nm (Trautmann et al., 1998, Trautmann et al., 1999, Frouin et al., 2019, Sontag-González and Fuchs, 2022). The red component is highly light-sensitive and thermally unstable and has been observed to increase with dose in several experiments (Krbetschek et al., 2000). This behavior has been attributed to luminescence from defect centers distinct from those responsible for the principal IR-RF emission, including centers associated with Fe-bearing defects or other trace-element substitutions. As irradiation proceeds, emission from these centers can grow even as the main IR-RF signal decreases. In addition, spectral overlap between emission bands can affect the apparent dose response behavior. At high doses, the principal IR-RF emission near 850-880 nm approaches a plateau, while the red emission near 710 nm may continue to increase. If the detection window includes part of this red component, the measured signal can appear to increase even though the population of the main IR-RF traps is decreasing. Such overlap effects have been noted in previous multi-spectral RF studies and in experimental observations of volcanic feldspars (e.g., Fattahi and Stokes, 2003). The behavior observed here is therefore consistent with a superposition of emission components: the principal IR-RF band, which decreases toward a plateau as traps fill, and a secondary red component that can increase with dose.

Across the two near-infrared detection windows (850 and 880 nm), both the emission intensity and the plateau dose strongly varies amongst the feldspar types. Albite and microcline show the highest initial IR-RF intensities and decrease monotonically with dose toward a plateau. Microcline displays a larger dynamic range at 850 nm, where the signal decays

https://doi.org/10.5194/egusphere-2026-2868
Preprint. Discussion started: 12 June 2026

gradually and approaches a plateau at ~4,000 Gy (compared with ~2,000 Gy at 880 nm). In contrast, albite shows the larger dynamic range at 880 nm, where the initial intensity is highest and the signal decreases sharply to a plateau by ~500 Gy (compared with ~800 Gy at 850 nm). Sanidine (TCs) behaves differently from microcline: its dose response decreases only in the 880 nm window, where the signal is low and approaches a plateau near ~500 Gy. Anorthite (Ca-rich) and labradorite (intermediate) yield low-intensity signals in both windows that remain near-flat and only slightly above background across the measured dose range, indicating weak and minimally dose-dependent responses.

To evaluate whether the sanidine behavior observed for TCs reflects an isolated case or a broader characteristic of sanidine, additional sanidine samples (ACs, FCs, and cima) were measured using the 850 nm filter (Fig. 5). All samples yield measurable IR-RF signals, but both the magnitude and the shape of the DRCs vary amongst the samples. The FCs, TCs and cima sanidines all display IR-RF intensities that increase with dose, whereas the ACs show a slight decrease despite a high initial intensity.

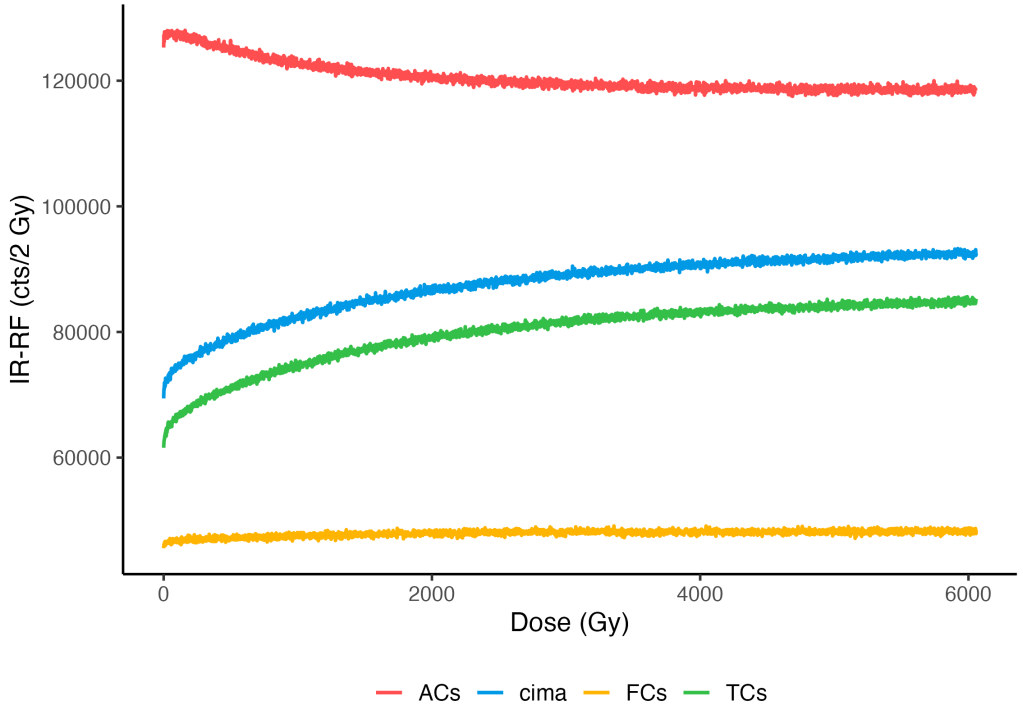

Figure 5: IR-RF dose response curves (DRCs) of sanidine samples detected through an 850/30 nm filter. Alder Creek (ACs) is plotted in red, Peach Springs Tuff (cima) in blue, Fish Canyon Tuff (FCs) in yellow, and Taylor Creek (TCs) in green.

The contrasting 850-880 nm IR-RF dose response behavior observed between microcline and sanidine, together with variability among the sanidine samples at 850 nm, suggests that the IR-RF response is controlled by more than bulk feldspar

https://doi.org/10.5194/egusphere-2026-2868
Preprint. Discussion started: 12 June 2026

composition. Source rock type alone does not fully explain the observed differences in IR-RF behavior: sanidine from the FCs crystal-rich dacitic ignimbrite, as well as the cima and TCs rhyolitic sources, exhibits increasing IR-RF DRCs, whereas the rhyolitic source of the ACs sanidine exhibits a slight decrease. Although microcline and sanidine share a K-rich endmember composition, they differ in crystal structure and formation temperature, which could modify defect populations and trap characteristics. In addition, sanidine populations can exhibit substantial crystal-to-crystal and intra-crystal heterogeneity in K/Na and trace-element distributions, including zoning in elements such as Ba, strontium (Sr), and Pb, with variable contributions from other Fe-bearing components. Grain-scale heterogeneity may also arise from melt inclusions or other micro-inclusions that are common in volcanic feldspars and can contribute additional emission components or local quenching. These factors provide plausible mechanisms for why some natural sanidine samples show an increasing DRCs, detected with the 850 nm filter, whereas one showed a decreasing behavior, motivating more targeted single-grain measurements.

3.2.2 Synthetic multigrain aliquot reconstruction

The variability observed among feldspar types and among sanidine standards implies that multi-grain aliquots may represent mixtures of grains with contrasting IR-RF behaviors, with the potential to distort the apparent dose response curve. This effect has already been illustrated quantitatively by Sontag-González et al. (2024), who simulated theoretical multi-grain aliquots by summing stretched-exponential dose response functions representing a “desired” decreasing-grain population (category no. 1) and an increasing-grain population (category no. 2). Their simulations (their Fig. 3) show that even a modest contribution of anomalous grains (~20 % of the total signal) already modifies the curvature and reduces the apparent saturation level of the summed curve, while larger contributions (> 50 %) can dominate the DRC shape entirely.

Here, we test this conceptual result experimentally using controlled mixed-grain aliquots. Synthetic aliquots were prepared to quantify how grains with contrasting IR-RF behaviors modify the microcline DRC, specifically its signal intensity, curvature and high-dose behavior. Multi-spectral measurements indicate that the microcline sample has a relatively high signal intensity and a larger dynamic range in the 850 nm detection window. All mixing experiments were therefore performed using the 850 nm filter to maximize sensitivity changes in the microcline response and maintain consistent detection conditions across aliquots.

In optically stimulated luminescence (OSL), saturation point is often, although somewhat arbitrarily, approximated as the $2D_0$ value (Wintle and Murray, 2006). In IR-RF, however, saturation is more difficult to define because the signal commonly decreases progressively with dose and may not reach a sharply defined plateau within the measured dose range. Consequently, the definition and interpretation of IR-RF saturation remain an active topic of discussion (e.g., Murari et al., 2018; Murari et al., 2021; Kreutzer et al., 2022; Sontag-González et al., 2025). To allow consistent comparison, IR-RF DRCs were fitted using the stretched exponential function proposed by Erfurt and Krbetschek (2003b), and the dose corresponding

https://doi.org/10.5194/egusphere-2026-2868
Preprint. Discussion started: 12 June 2026

to 95% of the fitted asymptotic level (D95) was calculated for each curve and used as a reference point for comparison (Fig S8). We use D95 here as a practical comparison metric rather than as a direct analogue to the $2D_0$ criterion. Although ~86% of saturation is commonly used in OSL to represent saturation onset for a simple saturating exponential, IR-RF curves fitted with a stretched exponential function commonly approach the asymptote more gradually. D95 therefore provides a conservative and reproducible reference point in the high dose region of the fitted curve for comparing apparent saturation behavior across feldspar compositions and synthetic mixtures, even where the absolute saturation point is not uniquely defined.

Figure 6 presents the DRCs measured with a PMT obtained for a single microcline grain, a single albite grain, and the combined one-microcline + one-albite aliquot. Because absolute IR-RF intensities noticeably differ between the two feldspars, the curves were normalized to their respective minimum and maximum values to enable comparison of the DRC shape. The combined-grain curve lies between the two endmembers, indicating that the integrated response reflects an average of the component grain behaviors under the 850 nm detection window. The apparent plateau dose was quantified using the D95 criterion. Microcline reaches D95 at ~2350 Gy, whereas albite reaches D95 at ~1360 Gy; the combined aliquot yields an intermediate value of ~1780 Gy, corresponding to an apparent reduction of ~24 % relative to microcline alone.

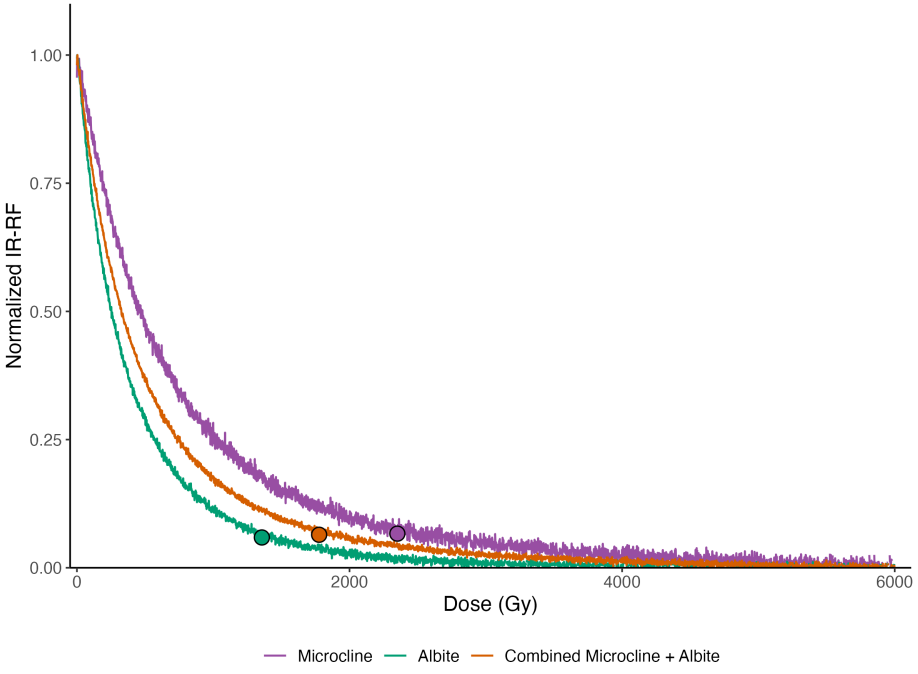

Figure 6: Dose response curves (DRCs) for microcline (purple), albite (green), and synthetic microcline + albite (orange) aliquots. The IR-RF DRCs are normalized to the tail averaged minimum and maximum values to illustrate relative differences in the shape of the DRC. The round symbols denote the dose that corresponds to 95% saturation (D95) for each aliquot.

https://doi.org/10.5194/egusphere-2026-2868
Preprint. Discussion started: 12 June 2026

Since the same grains were measured first as single grains and then in combined configurations, we evaluated whether repeated IR-RF measurement and bleaching could modify the DRC shape through sensitivity change. To do so, the IR-RF measurement of a single-grain microcline aliquot was repeated six consecutive times under identical irradiation and bleaching conditions. IR-RF measurements were conducted at 70 °C following Frouin et al. (2017) to a total dose of 6,000 Gy, and the aliquot was bleached for 6 h between cycles using the solar simulator integrated in the reader. Figure 7a shows the six DRCs, and Figure 7b summarizes the corresponding D95 values. Across cycles, the D95 values remain within ±10% of the mean, indicating that the DRC shape and apparent plateau dose are reproducible under repeated measurement. Taken together, these results indicate that the D95 shift observed (Fig. 6) for the combined microcline + albite aliquot is not explained by repeated measurement effects and is instead attributable to combining grains with different IR-RF dose response characteristics.

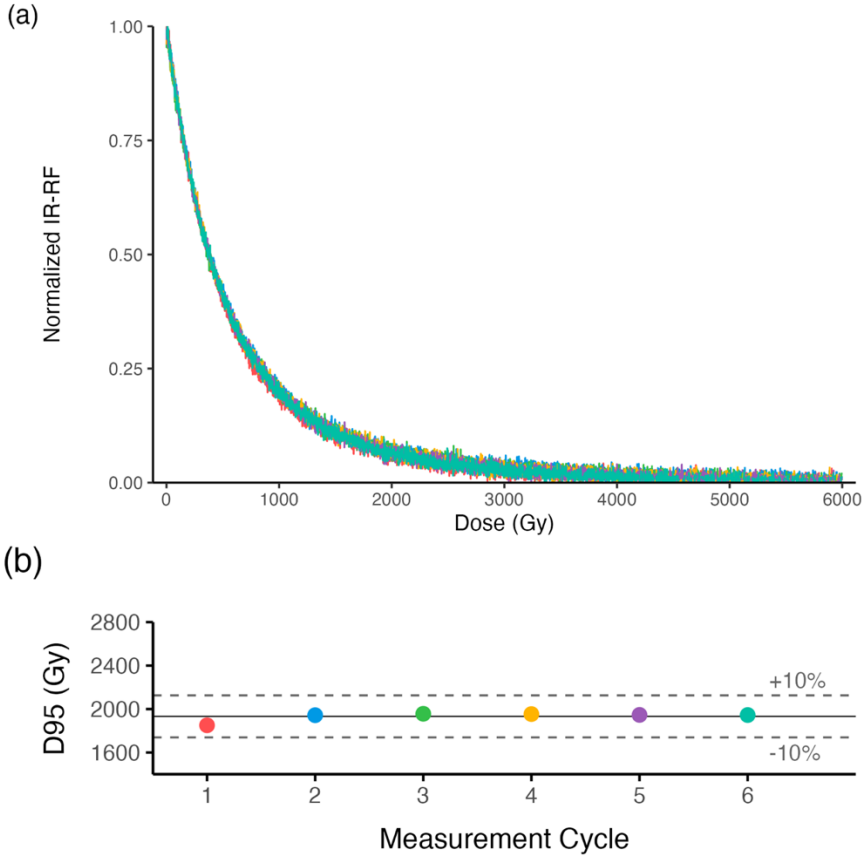

Figure 7: Microcline sensitivity drift experiment. (a) Dose response curves (DRCs) of one grain of microcline across six successive measurement cycles. (b) The dose that corresponds to 95% saturation (D95) for each cycle's DRC, illustrating very minimal sensitivity change across the cycles. The solid line represents the average D95 value across the six cycles, and the dashed lines highlight ± 10% of the average D95 value.

https://doi.org/10.5194/egusphere-2026-2868
Preprint. Discussion started: 12 June 2026

We then measured a combined aliquot consisting of a single microcline grain and four anorthite grains mounted together on a Lexsyg cup. Multiple anorthite grains were included to compensate for the relatively weak IR-RF emission of anorthite relative to microcline. Under the 850 nm detection window, the resulting one-microcline + four-anorthite DRC is indistinguishable from that of microcline alone, with no measurable change in curve shape or apparent saturation behavior. The data are not shown because the curves overlap within plotting resolution and cannot be visually distinguished when displayed together.

Figure 8 presents the DRCs for an individually placed single grain of microcline grain, a single sanidine (TCs) grain, the combined one-microcline + one-sanidine (TCs) aliquot, and the combined one-microcline + three-sanidine (TCs) aliquot. With increasing sanidine content, the initial rise in the IR-RF signal becomes more pronounced. Similar early-dose features have been previously reported and described as an initial 'bump', but their origin remains unresolved (e.g., Schilles, 2002; Buylaert et al., 2012; Frouin et al., 2014; Huot et al., 2015; Frouin et al., 2017; Murari et al., 2021). Based on simulations, Sontag-González et al. (2025) suggested that this initial 'bump' originates from signal contamination. Our controlled mixing results confirm that, at least in part, the systematic amplification of this rise can be produced by adding grains with different IR-RF dose response shapes and a lower effective dynamic range than microcline.

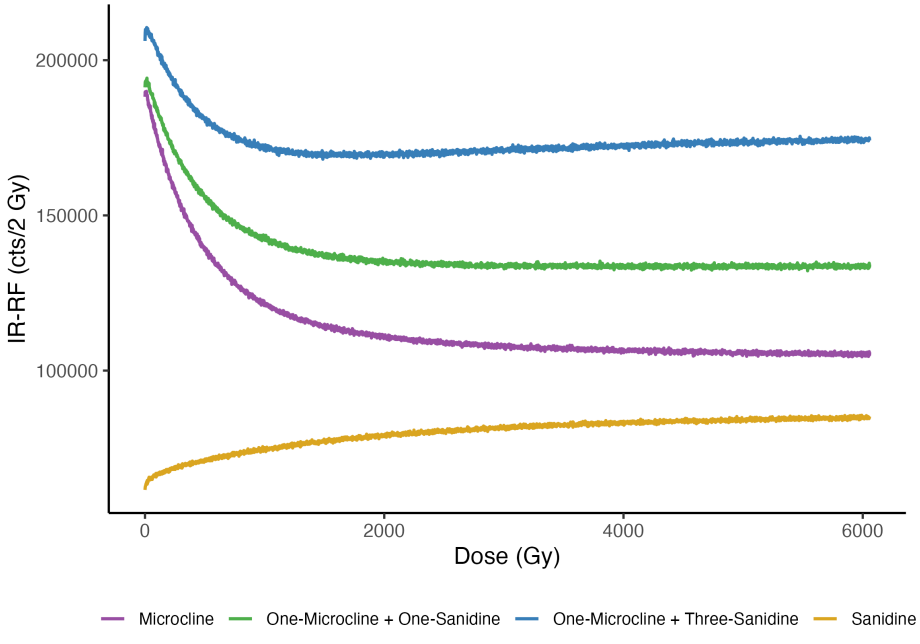

Figure 8: Dose response curves (DRCs) for a single-grain of microcline (purple), a single-grain of the TCs sanidine sample (yellow), and synthetic microcline + sanidine aliquots composed of one microcline + one sanidine grain (green) and one microcline + three sanidine grains (blue).

https://doi.org/10.5194/egusphere-2026-2868
Preprint. Discussion started: 12 June 2026

As in the one-microcline + one-albite experiment, combining grains shifts the DRC toward earlier apparent saturation. Microcline alone reaches D95 at ~2,350 Gy, whereas the combined one-microcline + one-sanidine aliquot reaches D95 at ~1,540 Gy, corresponding to an apparent reduction of ~35%. Increasing the sanidine contribution further accentuates this effect: the combined microcline + three-sanidine aliquot yields D95 of ~872 Gy, or ~63% lower than microcline alone. Together, these results show a progressive shift toward earlier apparent saturation with increasing sanidine content, demonstrating that mixing K-feldspar polymorphs can substantially modify the IR-RF DRC curvature and plateau characteristics even when the aliquot remains K-rich overall.

3.3 SR IR-RF

The progressive decrease in the D95 of microcline with increasing contribution from other feldspar grains (particularly sanidine and albite) indicates that grain-scale geochemistry can substantially alter both the curvature and the apparent saturation of a multi-grain IR-RF DRC. For dating applications, and especially for defining the saturation limit of a sample, one straightforward strategy is to move from bulk aliquots to single-grain measurements and apply selection criteria that retain grains with the largest dynamic range and the most suitable dose response behavior while excluding grains with anomalous or low-dynamic DRCs. In practice, however, PMT-based single-grain IR-RF measurements are largely time intensive and difficult to scale to the number of grains required to precisely date a natural sample. Spatially resolved IR-RF (SR IR-RF) provides a scalable alternative by enabling the simultaneous detection of numerous individual grains in a single measurement. This approach has only recently been introduced for IR-RF measurements (Mittelstraß and Kreutzer, 2021; Kumar et al., 2026) and opens the possibility of screening large numbers of grains in a way that was previously impractical with conventional single-grain IR-RF protocols. In the following, we evaluate the use of SR IR-RF as a screening tool to identify and classify grains according to their regenerative IR-RF dose response behavior, with the goal of supporting grain selection for D_e estimation and constraining sample-specific saturation limits.

3.3.1 SR IR-RF of the custom sample holder

Because our objective is to measure the same individual grains sequentially with SR IR-RF and synchrotron-based µ-XRF, we required a sample holder compatible with both techniques while preserving grain orientation. Conventional mounting techniques proved to be unsuitable; grains mounted on carbon tape on polystyrene slides (Sontag-González et al., 2024) were prone to loss during transport, whereas embedding grains in epoxy prevented subsequent IR-RF measurements. Standard Risø aluminum single-grain discs functioned well for SR IR-RF but generate background fluorescence during µ-XRF mapping and cannot be modified without permanently damaging the disc. To address these constraints, we developed a custom single-grain holder that reproduces the geometry of a Risø disc while being suitable for synchrotron analysis. A silicone mold ('BBDINO' mold-making kit) of a standard Risø single-grain disc was produced and used to cast interchangeable discs from 'KISREL' UV-cured resin. The resin was cured for 1 h in a solar simulator (UVACUBE400) equipped with a SOL500 lamp filtered with

https://doi.org/10.5194/egusphere-2026-2868
Preprint. Discussion started: 12 June 2026

an H1 filter glass (transmission range from 315 to 800 nm). Once cured, the resin disc was removed from the silicone mold and closely examined for imperfections or impression of bubbles. The grains were then loaded into the single grain disc and checked under a microscope to ensure each hole only had 1 grain. This approach produced cost-effective sample holders with the same geometry as a Risø single-grain disc while allowing for the sequential back-and-forth measurements of the IR-RF signal and μ-XRF mapping of the same gains, in the same orientation, all on one sample holder.

SR IR-RF tests showed that the resin holder introduces no significant signal during RF_{70} measurements. Thermal-conductivity tests using quartz TL peaks indicated that, although heat transfer through the resin is slower than in metal holders, the standard heating protocol is sufficient for the grains to reach the intended temperature (Fig S9).

3.3.2 SR IR-RF of natural samples

For the natural samples (X7363 and X7468), the SR IR-RF measurements were conducted using an RF_{70} protocol with a 5 s (~0.2 Gy) channel width, and exposure set to 4.5 s for a total irradiation dose of 3,075 Gy. Following the analysis protocol pioneered by Mittelstraß and Kreutzer (2021), each grain was marked as a region of interest (ROI) in ImageJ using the SR-RF macro. Each grain was assigned to a category (1-3) based on the shape of its regenerative IR-RF DRC. The mean signal within the first 500 Gy was compared to the mean signal over the last 1000 Gy of the measurement. Grains that display a decrease in signal intensity with increasing dose were classified as category 1, those that increase in signal intensity with increasing dose were classified as category 2, and those grains that show little or no change in signal intensity (a relatively flat response) were classified as category 3.

Both samples X7363 and X7368 contained grains that represent all three categories; however, the relative proportion of each category differs between the two samples. For sample X7363, ROIs were defined for 63 grains, of which, ~13% were classified as category 1, 27% as category 2, and 60% as category 3 (Fig S10). The regenerative IR-RF DRCs exhibited considerable differences in shape, even among the category 1 grains (Fig S11). For sample X7368, 48 ROIs were defined, of which ~46% were classified as category 1, 27% as category 2, and 27% as category 3. As observed for sample X7363, category 1 grains from sample X7368 exhibit grain-to-grain variability in the shape of their IR-RF DRCs.

Samples X7363 and X7368 were then polished down into the center of the grain and re-measured with SR IR-RF to evaluate the influence of the surface coating on the IR-RF DRC. The SR IR-RF measurements were conducted as described above; however, initial measurements indicated the 5 s channel size was too short to obtain DRCs from dimmer grains. While this change was initially unexpected, the polishing processes effectively removed approximately half of the grain mass, potentially reducing the measured IR-RF signal intensity. Here, we increased the channel size to 50 s (~2 Gy) and repeated the measurement. With the change in channel size and extended time between measurements (>6 months; machine background changes), we cannot comment on changes in the intensity of the IR-RF signal. However, for both samples, we found very

https://doi.org/10.5194/egusphere-2026-2868
Preprint. Discussion started: 12 June 2026

minimal differences in the shape of the IR-RF DRC. Figure 3 illustrates the IR-RF DRCs for category 1, 2, and 3 grains from sample X7363, shown for both the whole and polished grains. Here, we observe minimal visual differences between the whole and polished grains, indicating that the increasing "contaminated" IR-RF is unlikely to be caused by a surface coating. Instead, it is likely linked to an intrinsic grain property (e.g., bulk geochemistry and crystal structure).

4 Discussion

4.1 Implications of mineralogical mixing and grain heterogeneity on apparent IR-RF saturation

This study set out to test a simple but consequential point for IR-RF dating: the DRC measured on a multi-grain aliquot is not necessarily a property of a "sample" but can be a resulting average of grains with different mineralogy, defect population, and luminescence efficiency. Three observations support this:

First, multi-spectral single-grain measurements on reference feldspars confirm that the IR-RF response is not uniform across feldspar endmembers or across feldspar polymorphs. At 850 and 880 nm, albite and microcline produce the highest initial intensities and display an expected monotonic decrease with dose towards a plateau, but their apparent D95 doses differ substantially. Ca-rich feldspars (anorthite, labradorite) yield weak, minimally dose-dependent signals. Sanidine, despite being K-rich, behaves inconsistently across samples and can show increasing or decreasing DRCs depending on the sample and detection window. Similar complexities have been reported for infrared stimulated luminescence (IRSL) of feldspars, where volcanic feldspars typically exhibit high anomalous fading rates and are often regarded as poor candidates for dating (e.g., Wintle, 1973; Li et al., 2016). One possible explanation for the distinct RF behavior observed in some alkali feldspar is the presence of a thermoluminescence (TL) emission in the less-studied red region of the spectrum, centered near 710 nm (Visocekas and Zink, 1973; Fattahi and Stokes, 2003; Visocekas et al., 2014). Together, these observations indicate that the IR-RF DRC shape and dynamic range depend on more than bulk chemistry alone and likely reflect crystal structure and grain-scale heterogeneity.

Second, controlled mixed-grain experiments demonstrate that adding a small number of grains with contrasting IR-RF behavior can measurably modify the apparent saturation dose of an otherwise "well-behaved" microcline DRC when measured as a combined aliquot. Combining one microcline grain with one albite grain shifts the DRC toward earlier apparent saturation (D95 reduced by ~24% relative to microcline alone). Combining microcline with sanidine produces an even stronger effect, with D95 reductions of ~35% (one sanidine) and ~63% (three sanidines). In contrast, adding four anorthite grains produced no measurable effect on the microcline DRC under the 850 nm detection window, consistent with the low intensity and near-flat DRC of Ca-rich feldspars in that window.

https://doi.org/10.5194/egusphere-2026-2868
Preprint. Discussion started: 12 June 2026

Third, SR IR-RF measurements on natural samples X7363 and X7368 show that both samples contain grains with decreasing (category 1), increasing (category 2), and near-flat (category 3) regenerative DRCs, with different category proportions between samples. In both samples, nearly a third of grains were described as category 2, so that the IR-RF signal of multi-grain aliquots can be expected to be compromised. Importantly, polishing grains and repeating SR IR-RF measurements produced minimal visual changes in DRC shape, indicating that increasing or anomalous IR-RF behavior is unlikely to be explained solely by surface coatings. This result is another evidence that intrinsic grain properties are important for IR-RF dating purposes and further motivates single-grain scale approaches for defining sample-specific saturation characteristics.

4.2 Linking IR-RF DRC categories to composition

The 10 keV synchrotron μ-XRF maps provide a qualitative view of grain-scale elemental distributions and offer a first-order test of whether IR-RF DRC categories map cleanly onto a simple compositional discriminator. Plotting the natural-grain μ-XRF detections by the IR-RF category (Fig. 08) shows that K, Ca, and Fe are detected across both category 1 and category 2 grains, and that the presence or absence of these elements alone does not uniquely explain the observed DRC differences. Ba appears more consistently in category 1 grains than in category 2 grains in the subset analyzed, which is broadly consistent with prior observations that grains producing the “desired” decreasing DRC often coincide with K-rich compositions containing detectable Pb and Ba and relatively low Fe (Sontag-González et al., 2024). However, the present dataset also makes clear that an elemental presence or absence criterion is not sufficient on its own to predict the IR-RF category.

Two factors likely contribute to this limited separability. First, the μ-XRF maps used here are qualitative, and grain thickness and topography prevent direct comparison of relative intensities among grains. A grain that “contains Fe” in a detection sense can still differ substantially in the abundance, spatial distribution, and oxidation state of Fe-bearing centers that may influence luminescence. Second, the controls on IR-RF DRC shape are very likely multi-dimensional: polymorph specific defect structures and Al-Si ordering could modify trap populations even at similar bulk compositions. Trace elements can act as activators or quenchers depending on their lattice site and valence and micro-inclusions can contribute additional emission components that shift the apparent DRC. In this context, the absence of a unique μ-XRF signature by category is not a negative result but indicates that a simple geochemical composition is unlikely to explain IR-RF heterogeneity, and that predictive models of IR-RF behavior will require joint consideration of mineralogy, structure, and spatially resolved chemistry.

4.3 D95 as a practical screening metric in natural samples: promise and limits

A central motivation for this study is methodological: if grain-scale heterogeneity can bias bulk DRC curvature and apparent plateau dose, then a practical dating workflow needs a way to (i) identify grains that best represent the dosimetric IR-RF

https://doi.org/10.5194/egusphere-2026-2868
Preprint. Discussion started: 12 June 2026

population and (ii) quantify saturation characteristics in a sample specific way. D95 is attractive because it converts a full DRC into a single, reproducible parameter, allowing comparison across grains and mixtures even when the DRC does not reach a sharply defined plateau.

The mixed-grain experiments demonstrate that D95 is sensitive to mineralogical mixing and can capture progressive shifts toward earlier apparent saturation as "contaminant" grains contribute to the integrated signal. This is precisely the behavior expected if the bulk DRC reflects a weighted sum of grains with different plateau doses. In that sense, D95 is not merely a descriptive statistic. It behaves like an operational proxy for how much dosimetric capacity remains in the measured grain population under a given protocol and detection window.

The natural samples provide a more stringent test. SR IR-RF measurements show broad within-sample D95 variability even after restricting analysis to grains that display the desired decreasing regenerative behavior (category 1). For category 1 grains in X7363, D95 values average 1,870 Gy with a standard deviation of 462 Gy (median of 1997 Gy). For category 1 grains in X7368, the corresponding values are 2,101 ± 441 Gy (median of 2132 Gy). These spreads are substantial relative to the mean plateau dose and demonstrate that "well behaving" DRC shape alone does not guarantee uniform dosimetric capacity. The medians lying above the means in both samples indicate that a minority of category 1 grains still exhibit relatively low D95 values, which would tend to bias a bulk multi-grain signal toward earlier apparent saturation if included without screening.

This motivates a two-step screening approach in natural samples. Qualitative DRC classification provides a first-pass filter to remove grains with increasing or near-flat regenerative behavior (categories 2-3). Within the remaining category 1 population, D95 provides a quantitative criterion to prioritize "high-capacity" grains with later apparent saturation, which are the grains most relevant for extending dating limits and constraining sample-specific saturation behavior. However, confirming this as a robust selection criterion will require tests on independently well-dated and/or well-constrained stratigraphic samples to determine whether category-plus-D95 screening improves D_e reproducibility, reduces inter-aliquot scatter, and produces accurate stratigraphically consistent ages.

5. Conclusion

This work supports three practical conclusions for IR-RF dating. First, DRCs are not purely sample properties. Bulk aliquot DRC curvature and apparent plateau dose can shift substantially with grain mixing, particularly when contaminant grains contribute non-trivially to the detected signal. Second, SR IR-RF provides a scalable way to characterize grain-to-grain variability and to develop sample specific screening criteria. Combining DRC shape classification with D95 distributions appears to be a promising approach for identifying grains with higher dynamic range and later apparent saturation. Third, bulk chemistry alone does not explain anomalous DRCs. Qualitative μ-XRF mapping at 10 keV indicates that simple element

https://doi.org/10.5194/egusphere-2026-2868
Preprint. Discussion started: 12 June 2026

presence or absence does not uniquely predict DRC category, and polishing experiments argue against a purely surface-controlled origin for anomalous DRC behavior. Together, these results imply that a robust IR-RF saturation assessment will likely require integrating mineralogical identification, structural constraints, and spatially resolved grain-interior chemistry. To build on these results, future work should prioritize developing a quantitative, transferable screening criterion that can be applied across datasets to preferentially accept high-capacity K-feldspar grains (microcline/orthoclase) while excluding grains prone to early apparent saturation or anomalous behavior (e.g., albite and sanidine) and validating this workflow against independently well-dated and/or stratigraphically constrained sequences.

Data availability

The original data used to produce the μ-XRF maps, and all IR-RF datasets are available online at https://doi.org/10.5281/zenodo.19488227 (Grandfield et al., 2026).

Author contribution

TG, MF, JT, and JLS designed the experiments and prepared the samples. TG, MSG, RK carried out the IR-RF measurements. TG, MF, JT, AK, and VC carried out the μ-XRF measurements. TG analyzed the results. HN provided reference samples. TG prepared the manuscript with contributions from all authors. MF, JT, MSG, and JLS obtained funding.

Competing interests

The authors declare that they have no conflict of interest.

Acknowledgements

We would like to thank Dr. E. Troy Rasbury, Dr. Sidney Hemming, and Kevin Hatton for their help with acquiring the sanidine samples. This research used the 5-ID (SRX) beamline of the National Synchrotron Light Source II; a U.S. Department of Energy (DOE) Office of Science User Facility operated for the DOE Office of Science by Brookhaven National Laboratory under Contract No. DE-SC0012704.

Financial support

This work has been supported by a National Science Foundation Archaeometry Grant (award no.2309407); a Stony Brook University-Brookhaven National Laboratory 2022 Seed Grant (grant no. 94508); and a Natural Environment Research Council (grant number NE/T001313/1). TG was supported by an NSF-BSF grant (grant no. 2021219) and a Stony Brook University Center for Inclusive Education Research and Professional Development Award. MSG was supported by the European Union's Marie Skłodowska-Curie fellowship (grant no. 101206436)

https://doi.org/10.5194/egusphere-2026-2868
Preprint. Discussion started: 12 June 2026

References

Buylaert, J.-P., Jain, M., Murray, A. S., Thomsen, K. J., and Lapp, T.: IR-RF dating of sand-sized K-feldspar extracts: A test of accuracy, Radiat. Meas., 47, 759-765, https://doi.org/10.1016/j.radmeas.2012.06.021, 2012.

Cebula, G.T., Kunk, M.J., Mehnert, H.H., Naeser, C.W., Obradovich, J.D., and Sutter, J.F., 1986, The Fish Canyon Tuff, a potential standard for the 40Ar-39Ar and fission-track dating methods [abstract], in Sixth international conference on Geochronology, cosmochronology and isotope geology: Cambridge, United Kingdom, European Union of Geosciences, Terra Cognita v. 6, issue 2, p. 139-140, 1986

Duffield, W.A., Dahymple, G.B.: The Taylor Creek Rhyolite of New Mexico: a rapidly emplaced field of domes and flows, Bull. Volcanol., 52, 475-478, https://doi.org/10.1007/BF00268927,1990.

Erfurt, G. and Krbetschek, M. R.: Studies on the physics of the infrared radioluminescence of potassium feldspar and on the methodology of its application to sediment dating, Radiat. Meas., 37, 505-510, https://doi.org/10.1016/S1350-4487(03)00058-1, 2003a.

Erfurt, G. and Krbetschek, M. R.: IRSAR - A single-aliquot regenerative-dose dating protocol applied to the infrared radiofluorescence (IR-RF) of coarse-grain K-feldspar, Ancient TL, 21, 35-42, https://doi.org/10.26034/la.atl.2003.358, 2003b.

Frouin, M.: Les feldspaths comme support pour la datation par luminescence des gisements archéologiques et des séquences quaternaires d'Aquitaine, Ph.D. thesis, École Doctorale Montaigne Humanités, Université Bordeaux Montaigne, France, 391 pp., 10.70675/c7cc32f3z7150z468bza993z47118f93f4c9, 2014.

Frouin, M., Huot, S., Kreutzer, S., Lahaye, C., Lamothe, M., Philippe, A., and Mercier, N.: An improved radiofluorescence single-aliquot regenerative dose protocol for K-feldspars, Quat. Geochronol., 38, 13-24, https://doi.org/10.1016/j.quageo.2016.11.004, 2017.

Frouin, M., Kumar, R., Kook, M., Buylaert, J.-P., and Jain, M.: Further investigation on IRRF and IRPL, 29/10/2019, DLED conference, 2019.

Grandfield, T., Sontag-González, M., Kumar. R., Thieme, J., Kiss, A. M., Schwenninger, J.-L., Nekvasil, H., Castle, V., Frouin, M. , Zenodo [dataset], https://doi.org/10.5281/zenodo.19488227, 2026.

Huot, S., Frouin, M., and Lamothe, M.: Evidence of shallow TL peak contributions in infrared radiofluorescence, Radiat. Meas., 81, 237-241, https://doi.org/10.1016/j.radmeas.2015.05.009, 2015.

Jain, M., Sohbati, R., Guralnik, B., Murray, A. S., Kook, M., Lapp, T., Prasad, A. K., Thomsen, K. J., and Buylaert, J. P.: Kinetics of infrared stimulated luminescence from feldspars, Radiat. Meas., 81, 242-250, https://doi.org/10.1016/j.radmeas.2015.02.006, 2015.

Jarosewich, E., Nelen, J. A., and Norberg, J. A.: Reference Samples for Electron Microprobe Analysis. Geostandards Newsletter 4, p. 43-47, https://doi.org/10.1111/j.1751-908X.1980.tb00273.x,1980.

Jarosewich E.: Smithsonian Microbeam Standards, J. Res. Natl. Inst. Stand. Technol. 107(6):681-5, doi:10.6028/jres.107.054, 2002.

Kirsh, Y. and Townsend, P. D.: Speculations on the blue and red bands in the TL emission spectrum of albite and

https://doi.org/10.5194/egusphere-2026-2868
Preprint. Discussion started: 12 June 2026

microcline, Int. J. Rad. Appl. Instrum. Part D. Nucl. Tracks Rad. Meas., 14, 43-49, https://doi.org/10.1016/1359-0189(88)90040-4, 1988.

Krbetschek, M. R., Trautmann, T., Dietrich, A., and Stolz, W.: Radioluminescence dating of sediments: methodological aspects, Radiat. Meas., 32, 493-498, https://doi.org/10.1016/S1350-4487(00)00122-0, 2000.

Kreutzer, S., Murari, M.K., Frouin, M., Fuchs, M., Mercier, N.: Always remain suspicious: a case study on tracking down a technical artefact while measuring IR-RF. Ancient TL 35, 20-30. doi:10.26034/la.atl.2017.510, 2017.

Kreutzer, S., Mercier, N., and Lamothe, M.: Infrared-radiofluorescence: Dose saturation and long-term signal stability of a K-feldspar sample, Radiat. Meas., 156, 106818, https://doi.org/10.1016/j.radmeas.2022.106818, 2022.

Kreutzer S, Burow C, Dietze M, Fuchs M, Schmidt C, Fischer M, Friedrich J, Mercier N, Philippe A, Riedesel S, Autzen M, Mittelstrass D, Gray H, Galharret J, Colombo M, Steinbuch L, de Boer A.d.: Luminescence: Comprehensive Luminescence Dating Data Analysis. R package version 1.1.1, https://r-lum.github.io/Luminescence/, 2025.

Kumar, R., Frouin, M., Sontag-González, M., Grandfield, T., Schwenninger, J.-L.: Spatially resolved infrared-radiofluorescence (SR IR-RF) measurements for single-grain feldspar dating., Rad. Phys. and Chem., 240, 113930, https://doi.org/10.1016/j.radphyschem.2026.113930, 2026.

Kumar, R., Martin, L. I. D. J., Poelman, D., Vandenberghe, D., De Grave, J., Kook, M., and Jain, M.: Site-selective mapping of metastable states using electron-beam induced luminescence microscopy, Sci. Rep., 10, 15650, https://doi.org/10.1038/s41598-020-72334-7, 2020.

Kumar, R., Kook, M., Murray, A. S., and Jain, M.: Towards direct measurement of electrons in metastable states in K-feldspar: Do infrared-photoluminescence and radioluminescence probe the same trap? Radiat. Meas., 120, 7-13, https://doi.org/10.1016/j.radmeas.2018.06.018, 2018.

Li, B., Zhao, J.-X., Grün, R., Aubert, M., Ramli, M., Hakim, B., Saptomo, E. W.: IRSL dating of fast-fading sanidine feldspars from Sulawesi, Indonesia. Ancient TL, 34(2), 1-13. https://doi.org/10.26034/la.atl.2016.503, 2016.

Li, L., Yan, H., Xu, W., Yu, D., Heroux, A., Lee, W.-K., Campbell, S. I., and Chu, Y. S.: PyXRF: Python-based X-ray fluorescence analysis package, in: X-Ray Nanoimaging: Instruments and Methods III, SPIE Optical Engineering and Applications, 38-45, https://doi.org/10.1117/12.2272585, 2017.

Mittelstraß, D. and Kreutzer, S.: Spatially resolved infrared radiofluorescence: single-grain K-feldspar dating using CCD imaging, Geochronology, 3, 299-319, https://doi.org/10.5194/gchron-3-299-2021, 2021.

Murari, M. K., Kreutzer, S., and Fuchs, M.: Further investigations on IR-RF: Dose recovery and correction, Radiat. Meas., 120, 110-119, https://doi.org/10.1016/j.radmeas.2018.04.017, 2018.

Murari, M. K., Kreutzer, S., King, G. E., Frouin, M., Tsukamoto, S., Schmidt, C., Lauer, T., Klasen, N., Richter, D., Friedrich, J., Mercier, N., and Fuchs, M.: Infrared radiofluorescence (IR-RF) dating: A review, Quat. Geochronol., 64, 101155, https://doi.org/10.1016/j.quageo.2021.101155, 2021.

Nazaretski, E., Coburn, D. S., Xu, W., Ma, J., Xu, H., Smith, R., Huang, X., Yang, Y., Huang, L., Idir, M., Kiss, A. & Chu, Y. S.: A new Kirkpatrick-Baez-based scanning microscope for the Submicron Resolution X-ray Spectroscopy (SRX) beamline at NSLS-II. J. Synchrotron Rad., 29, 1284-1291, https://doi.org/10.1107/S1600577522007056, 2022.

https://doi.org/10.5194/egusphere-2026-2868
Preprint. Discussion started: 12 June 2026

Nielsen, J. E., Lux, D. R., Dalrymple, G. B., Glazner, A.: Age of the Peach Springs Tuff, Southeastern California and Western Arizona. J. Geophys. Research, 95, 571-580. https://doi.org/10.1029/JB095iB01p00571, 1990.

Ribbe, P.H.: Aluminum-Silicon order in feldspars; Domain textures and diffraction patterns. In: Ribbe, P.H. (ed.). Feldspar Mineralogy (second edition). Reviews in Mineralogy 2, 21-55, 10.2138/rmg.1983.2.2, 1983.

Riedesel, S., Kumar, R., Duller, G. A. T., Roberts, H. M., Bell, A. M. T., and Jain, M.: Site-selective characterisation of electron trapping centres in relation to chemistry, structural state and mineral phases present in single crystal alkali feldspars. J. Phys. Appl. Phys., 54, 385107, https://doi.org/10.1088/1361-6463/ac10d7, 2021.

Richter, D., Pintaske, R., Dornich, K., & Krbetscheck, M.: A novel beta source design for uniform irradiation in dosimetric applications. Ancient TL, 30(2), 57-64. https://doi.org/10.26034/la.atl.2012.464, 2012.

Richter, D., Richter, A., and Dornich, K.: LEXSYG - A new system for luminescence research, Geochronometria, 40, 220–228, https://doi.org/10.2478/s13386-013-0110-0, 2013.

Schilles, T.: Die Infrarot-Radiolumineszenz von Feldspäten und ihr Einsatz in der Lumineszenzdatierung, Ph.D., thesis, Heidelberg University, Germany, 149 pp., 10.11588/heidok.00001862, 2002.

Schilles, T., Habermann, J.:Radioluminescence dating: the IR emission of feldspar. Radiat. Meas. 32, 679e683. http://dx.doi.org/10.1016/S1350-4487(00) 00081-0, 2000.

Sontag-González, M. and Fuchs, M.: Spectroscopic investigations of infrared-radiofluorescence (IR-RF) for equivalent dose estimation, Radiation Measurements, 153, 106733, https://doi.org/10.1016/j.radmeas.2022.106733, 2022.

Sontag-González, M., Mittelstraß, D., Kreutzer, S., and Fuchs, M.: Wavelength calibration and spectral sensitivity correction of luminescence measurements for dosimetry applications: Method comparison tested on the IR-RF of K-feldspar, Radiat. Meas., 159, 106876, https://doi.org/10.1016/j.radmeas.2022.106876, 2022.

Sontag-González, M., Kumar, R., Schwenninger, J.-L., Thieme, J., Kreutzer, S., and Frouin, M.: Short communication: Synchrotron-based elemental mapping of single grains to investigate variable infrared-radiofluorescence emissions for luminescence dating, Geochronology, 6, 77-88, https://doi.org/10.5194/gchron-6-77-2024, 2024.

Sontag-González, M., Murari, M. K., Jain, M., Frouin, M., and Fuchs, M.: Further investigations into the accuracy of infrared radiofluorescence (IR-RF) and its inter-comparison with infrared photoluminescence (IRPL) dating, Geochronology, 7, 289-308, https://doi.org/10.5194/gchron-7-289-2025, 2025.

Trautmann, T., Krbetschek, M. R., Dietrich, A., and Stolz, W.: Investigations of feldspar radioluminescence: potential for a new dating technique, Radiat. Meas., 29, 421-425, https://doi.org/10.1016/S1350-4487(98)00012-2, 1998.

Trautmann, T., Krbetschek, M. R., Dietrich, A., and Stolz, W.: Feldspar radioluminescence: a new dating method and its physical background, J. Lumin., 85, 45-58, https://doi.org/10.1016/S0022-2313(99)00152-0, 1999.

Trautmann, T., Krbetschek, M. R., and Stolz, W.: A systematic study of the radioluminescence properties of single feldspar grains, Radiat. Meas., 32, 685-690, https://doi.org/10.1016/S1350-4487(00)00077-9, 2000.

Turrin, B.D., Donnelly-Nolan, J.M., Heam, B.C. Jr.:^{40}Ar/ ^{39}Ar ages from the rhyolite of Alder Creek, California: Age of the Cobb Mountain normal-polarity subchron revisited. Geology, 22, 25l-254, https://doi.org/10.1130/0091-7613(1994)022<0251:AAAFTR>2.3.CO;2 1994.

https://doi.org/10.5194/egusphere-2026-2868
Preprint. Discussion started: 12 June 2026

Visocekas, R., Zink, A.: Use of the far red TL emission band of alkali feldspars for dosimetry and dating. Quat. Sci. Rev. (Quat. Geochron.), 18, 271-278, https://doi.org/10.1016/S0277-3791(98)00059-6,1999.

Visocekas, R., Barthou, C., and Blanc, P.: Thermal quenching of far-red Fe3+ thermoluminescence of volcanic K-feldspars, Radiat. Meas., 61, 52-73, https://doi.org/10.1016/j.radmeas.2013.11.002, 2014.

Wintle, AG.: Anomalous Fading of Thermo-luminescence in Mineral Samples. Nature, 245, 143-144, https://doi.org/10.1038/245143a0, 1973.

Wintle AG, and Murray A.: A review of optically stimulated luminescence characteristics and their relevance in single-aliquot regeneration dating protocols. Radiat. Meas., 41, 369-391, https://doi.org/10.1016/j.radmeas.2005.11.001, 2006.

Zimmerer, M. J., McIntosh, W. C.: 40Ar/39Ar dating, sanidine chemistry and potential sources of the Las Tablas Tuff, northern New Mexico, in: Geology of the Tusas Mountains and Ojo Caliente Area, Koning, Daniel J.; Karlstrom, Karl E.; Kelley, Shari A.; Lueth, Virgil W.; Aby, Scott B., ed(s), New Mexico Geol. Soci, Guidebook, 62, 215-222, 2011